Journal of Power Sources 194 (2009) 908–919

Contents lists available at ScienceDirect

Journal of Power Sources

journal homepage: www.elsevier.com/locate/jpowsour

Physics-based modeling of a low-temperature solid oxide fuel cell with consideration of microstructure and interfacial effects

Kun Yuan, Yan Ji, J.N. Chung*

Department of Mechanical and Aerospace Engineering, University of Florida, Gainesville, FL 32611-6300, USA

ARTICLE INFO

Article history:
Received 18 April 2009
Received in revised form 19 May 2009
Accepted 20 May 2009
Available online 6 June 2009

Keywords:
Solid oxide fuel cell
Low temperature
Multi-scale modeling
Microstructure
Electrochemical transport
Composite electrode

ABSTRACT

The main objective of this paper is to develop a physical model for the simulation of heat/mass transport and electrochemical process in a solid oxide fuel cell. The model is then used to evaluate the effects of lowering the operating temperature for a solid oxide fuel cell. This model consists of two submodels, i.e., a micro-scale submodel and a macro-scale submodel. The macro-scale submodel is based on the continuum conservation laws. The micro-scale submodel addresses the complex relationships among the transport phenomena in the electrodes and electrolyte, which includes the transport of electron, ion, and gas molecules through the composite electrodes, electrolyte, and triple-phase boundary region. After integrating the two submodels, the dependence of electrochemical performance on the temperature, global geometrical parameter, and microstructures (porosity, volume fraction and composite ratio, etc.) were assessed.

Results demonstrate that for a reduced-temperature solid oxide fuel cell with composite electrodes, its performance is also lowered due to a higher ohmic loss in electrolyte and a slower electrochemical kinetics in the cathode. Among the various microstructure parameters for electrodes, the particle size and TPB length are the most important factors that dominate the performance of a reduced-temperature SOFC. In addition, optimal thicknesses for the electrodes exist. It is believed that the current work will provide a valuable model approach, which can be used to help understand the complex transport phenomena in electrodes and optimize the design of a reduced-temperature solid oxide fuel cell.

1. Introduction

The superior efficiency of a solid oxide fuel cell in comparison with other energy-conversion systems is due to its higher operation temperature, which may exceed 1000 °C in some designs [1,2]. As the operation temperature of a SOFC is reduced, the activation resistance in the electrodes and the ohmic resistance in the electrolyte will contribute to the majority of the total cell resistances [3–5]. For example, if reducing the operating temperature of a SOFC to 550–800 °C, the cathode resistance was 70–85% of the total cell resistance for anode-supported SOFCs with standard LSM-YSZ cathode on YSZ electrolyte [6]. However, lowering the operation temperature is an inevitable path for the commercialization of this technology, which allows for a broader choice of materials, reduces the fabrication cost, minimizes the interfacial diffusion between electrode and electrolyte, and improves the response time for start-up and shut-down period, etc. For this purpose, research has been focused on developing thin film electrolyte [7–9], adopting alternative electrolyte or electrodes with higher conductivity [10–12] and finding new fabrication processes for electrodes [13]. $Sm_{0.5}Sr_{0.5}CoO_{3-\delta}$ (SSC), $La_{1-x}Sr_xCo_{0.8}Fe_{1-y}O_{3-\delta}$ (LSCF) and $Ba_{0.5}Sr_{0.5}Co_{0.8}Fe_{0.2}O_{3-\delta}$ (BSCF) have been experimentally proven to provide a superior performance as a cathode material for SOFC or its combination with $Gd_{0.2}Ce_{0.8}O_{1.9}$ (GDC) and $Ce_{0.85}Sm_{0.15}O_2$ (SDC) to form a composite cathode [14–16]. For example, the measured total electrode area specific resistance is only 0.102 $\Omega\,cm^2$ at 600 °C for a cell with a SDC electrolyte thickness of 20 μm and a composite cathode (75 wt.% SCC + 25 wt.% SDC) [12]. Adding SDC particles to Ni is effective for improving the activity of Ni anode through increasing the TPB area and maintaining the appropriate porosity [11].

However, this kind of composite electrode exhibits a complex geometry/morphology, it is frequently a demanding task to predict how the interplay of materials properties and geometry (e.g., porosity, particle size, and electrode thickness) affects the polarization resistance. A micro-model, which focuses on the electrode and electrolyte region, is therefore crucial to understand the relations between performance and relevant microstructure parameters in much more detail [17–25]. For a lower temperature SOFC, the temperature becomes a crucial factor and even an insignificant variation in non-homogenous temperature distribution or flow field within a SOFC might substantially change the

* Corresponding author.
E-mail address: jnchung@ufl.edu (J.N. Chung).

0378-7753/$ – see front matter © 2009 Elsevier B.V. All rights reserved.
doi:10.1016/j.jpowsour.2009.05.045

Nomenclature

c	specific heat capacity [J kg^{-1} K^{-1}]
D_{ij}	binary mass diffusivity [m^2 s^{-1}]
$D_{k,i}$	effective Knudsen diffusion coefficient for component i [m^2 s^{-1}]
E	Nernst potential [V]
F	Faraday's constant, 96,486.7 [C mol^{-1}]
F_1	Forchheimer coefficient
ΔG	chemical potential [J mol^{-1}]
ΔH_{elec}	enthalpy change of reactions [J mol^{-1}]
i	local current [A m^{-2}]
$\mathbf{i}$	current vector [A m^{-2}]
$i_{tr}^{ca/an}$, i_o	exchange current density [A m^{-1} or A m^{-2}]
L	TPB length per unit volume [m^{-2}]
$\vec{J}$	diffusion mass flux vector
K	permeability of the porous medium [m^2]
k	thermal conductivity [W m^{-1} K^{-1}]
M_i	molar weight of component i [kg mol^{-1}]
n	number fraction
n_e	number of electron
N	total number of particles per unit volume
p	pressure [Pa]
P_ℓ	probability of ℓ-type conductors in the percolating cluster
P_i	partial pressure of component i [atm]
Q_{re}	heat generation from electrochemical reaction [W m^{-3}]
Q_{oh+act}	heat generation from ohmic and activation loss [W m^{-3}]
r	radius [m]
R_g	universal gas constant 8.3143 [J mol^{-1} K^{-1}]
R_{eff}	ohmic resistance [Ω]
S_i	net rate of production for component i
T	temperature [K]
$\vec{V}$	velocity vector [m s^{-1}]
X_i	molar fraction of component i
Y_i	mass fraction of component i
Z	coordination number

Greek letters

β	transfer coefficient
γ	contact angle [°]
ϕ	volume fraction
μ	viscosity [m^2 s^{-1}]
ε	porosity
σ	electrical conductivity [Ω^{-1} m^{-1}]
η_{act}	activation overpotential [V]
η_{ohm}	ohmic overpotential [V]
η_{con}	concentration overpotential [V]
λ	size ratio
ρ	density [kg m^{-3}]

Superscripts

air	air
fuel	fuel
ele	electrolyte
an	anode
ca	cathode
b	bulk
int	interface

Subscripts

eff	effective
el	electronic
i	components in gas mixture (fuel channel mixture: $i = H_2, H_2O$; air channel mixture: $i = O_2, N_2$)
io	ionic
TPB	triple-phase boundary

performance. Unfortunately, previous micro-models [26–29] cannot account for this temperature or geometry effect at macro-level (e.g., stack dimension) because of inherent model weakness and assumptions. Especially, when considering the goals of our model, i.e., how to optimize the entire cell design including global macro- and microstructure parameters, only few influencing factors in a model will lead to significant inaccuracies or errors in predicting overall SOFC performance. Therefore, it is desirable to develop a multi-scale model which has the capability of handling the transport mechanisms on different length scales at the same time.

The current study aims at developing a new multi-scale model, which will be employed to integrate a micro-scale submodel with a macro-scale submodel and account for transport mechanisms arising from different processes and length scales for a lower temperature SOFC. Recently, the authors have developed a multi-physics macro-model to investigate the effect of transport scale on the performance of a SOFC unit [30]. The macro-submodel is developed on the basis of the previous work. Then solution will be supplied to the micro-scale submodel as the global parameters. The micro-scale submodel establishes the complex relationships among the various transport phenomena in the pore level, which includes the transport of electron, ion and gas molecules through the electrodes, electrolyte and particularly at the three-phase boundary region. Finally, by integrating the two submodels to form a multiscale model, the dependence of electrochemical performance on the global parameters (temperature, thickness of electrodes) and microstructures (porosity, volume fraction, composite ratio, etc.) will be assessed for the entire fuel cell stack in a meaningful way.

2. General descriptions and model assumptions

A typical anode-supported planar SOFC single unit cell consisting of a thick layer of anode, a dense layer of electrolyte, a porous layer of cathode, and interconnects (or ribs) is illustrated in Fig. 1(a). Previous simulation results from the macro-model [30] have sufficiently demonstrated that the variations for temperature, velocity and concentration in the z-direction (normal to xy plane, refer to Fig. 1(a)) are insignificant if the rib thickness is small. So here, the rib thickness is assumed to be small and a two-dimensional model is considered for the concern of computational time. The schematic of the 2D computational model is shown in Fig. 1(b). To study the different physical processes at various length scales, the current model consists of two length scales: a macro-scale submodel and a micro-scale submodel. The macro-scale submodel is associated with the entire computation domain. While the micro-scale submodel is used only in the electrode and electrolyte regions. A Ni/SDC composite anode, a SDC electrolyte and a LSCF/SDC composite cathode are considered in the present simulation for simulating a lower temperature solid oxide fuel cell. In Fig. 1(b), the composite electrodes are modeled as a random packing system made of electronic particles (LSCF or Ni), ionic particles (SDC) and interstitial pores. LSCF is considered as a pure electronic conductor in our model; however, intrinsically it is a mixed conductor. Since the ionic conductivity of LSCF is lower than that of SDC, the LSCF may be assumed as a pure electronic conductor in a conservative approach. Current is conducted from particle to particle through the interface. The edge of electronic/ionic interface that makes contact with the

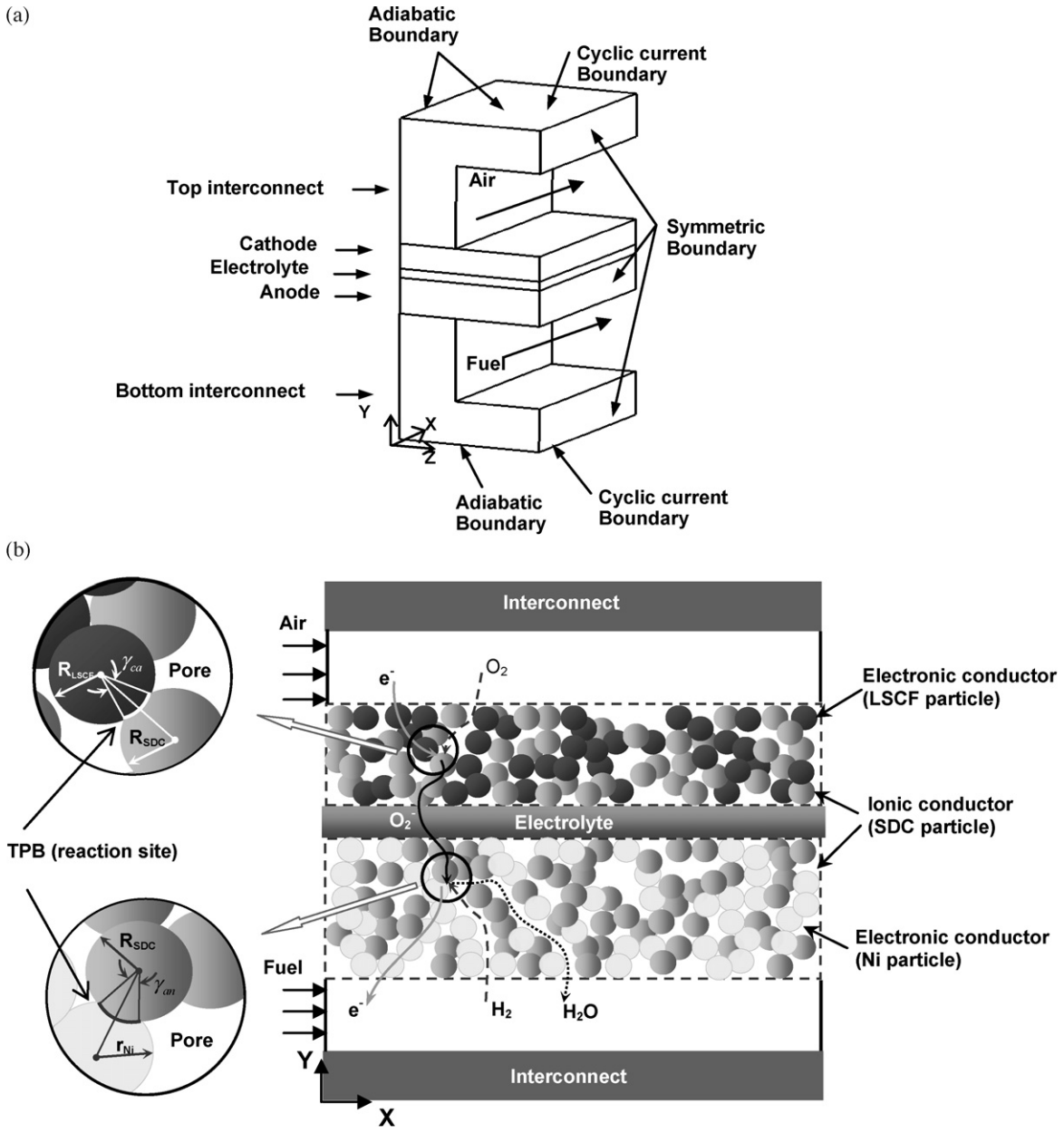

Fig. 1. Schematic diagrams of a planar solid oxide fuel cell: (a) 3D drawing of a unit cell and (b) 2D schematic of computational domain, structural modeling of a solid oxide fuel cell, and close-up of cermet TPB. The composite cathode (LSCF/SDC) and anode (Ni/SDC) are modeled by a random packing of binary particles (not to scale).

gas phase is the triple-phase boundary (TPB) which provides the reaction sites. Although a real porous microstructure is different from this random system, the previous studies have successfully proven its validity in predicting electrochemical performance for a composite electrode [18,19,21,31].

In the cathode region, oxygen which diffuses through the air channel and interconnected pores, is reduced somewhere in the vicinity of triple-phase boundary (TPB) region to oxygen ions via the overall half-cell reaction:

$$O_2(g) + 4e^- + 2V_O^{\cdot\cdot} \Leftrightarrow 2O_O^x \quad (1)$$

where $V_O^{\cdot\cdot}$ and O_O^x are vacancies and oxygen ions in the SDC phase. Likewise, the hydrogen reduction reaction in the TPB of the anode occurs as:

$$H_2(g) + O^{2-} \Leftrightarrow H_2O + 2e^- \quad (2)$$

The system terminal output is critically dependent on the activation, concentration, and ohmic polarizations and can be expressed as:

$$V_{cell} = E - \eta_{act}^{an+ca} - \eta_{con}^{an+ca+ch} - \eta_{ohm}^{an+ca+ele+inn} - \eta_{contact} \quad (3)$$

with the Nernst potential E is given below:

$$E = E_0 + \frac{R_g T}{2F} \ln\left(\frac{p_{H_2} p_{O_2}^{0.5}}{p_{H_2O}}\right) \quad (4)$$

where η_{act}^{an+ca} is the activation overpotential due to electrochemical reaction at TPB. $\eta_{con}^{an+ca+ch}$ is the concentration overpotential due to mass transport in the electrodes and channel flows. $\eta_{ohm}^{an+ca+ele+inn}$ is the ohmic overpotential across electrodes, electrolyte and interconnectors. $\eta_{contact}$ is the contact resistance. Actually, the internal current loss resulting from the dissipation of fuel passing through the electrolyte, and the electron conduction through the elec-

trolyte also causes the voltage loss. But its effect is usually not very important compared with the mentioned overpotentials, especially, in the case of higher-temperature cells, because the exchange current density is so much higher, such that the initial fall in voltage is not significant [1]. p_{H_2} and p_{H_2O} are the partial pressures of hydrogen and water in bulk channel flows, respectively. $E_0 = 1.2723 - 2.7645 \times 10^4 T$ depends on local temperature. However, it is rather difficult to clearly identify one kind of overpotential from others because they are highly inter-related in an actual energy transport process. Therefore, completely understanding and modeling those losses are critical to accurately predict the cell's electrochemical performance, which is one of the main objectives in the present work. Modeling is performed with the following assumptions:

- A planar cell with a co-flow configuration under the steady state condition is considered.
- Mass/heat transport and gradients in two-directions (2D) are considered.
- Energy transfer due to species diffusion in channel flows and porous layers is neglected. Because the single cell model represents a repeating cell structure in the center of a larger stack, cyclic boundary conditions for current are imposed at the boundaries of model domain. Walls at the periphery of the single cell are assumed to be adiabatic.
- For electrodes, each of the two conducting phases is considered as continuous and homogenous having an effective conductivity dependent on the micro-parameters.
- Identical and uniform catalyst activity throughout electrodes. Relevant electrode (anode SDC/Ni and cathode SDC/LSCF) parameters are extracted from the literatures.
- In view of that molecular diffusion and Knudsen diffusion are comparable in electrodes, both of them are considered together.

2.1. Macro-submodel

2.1.1. Governing equations

The macro-scale submodel has been developed [30,32,33] to simulate the thermal, flow and species fields in the entire computational domain. In the pure fluid region (channel flows), the Navier–Stokes equations describe the flow behavior. In the porous region (electrodes), flow is treated as laminar, incompressible and governed by the Brinkman–Forchheimer extended Darcy model. The conservation equations of mass, momentum, energy and species for fluids in both pure fluid region and porous domain are:

$$\nabla \cdot (\rho_f \vec{V}) = 0 \tag{5a}$$

$$\frac{\rho_f}{\varepsilon}\nabla \cdot (\vec{V}\vec{V}) = -\frac{\nabla p}{\varepsilon} + \frac{\mu_f}{\varepsilon}\nabla^2 \vec{V} - \zeta\left(\frac{\mu_f}{K}\vec{V} + \frac{\rho_f F_1 \varepsilon}{\sqrt{K}}\left|\vec{V}\right| \cdot \vec{V}\right) \tag{5b}$$

$$\nabla \cdot (\varepsilon \rho_f c_f \vec{V} T) = \nabla \cdot (k_{eff} \nabla T) + Q_{re} + Q_{oh+act} \tag{5c}$$

$$\nabla \cdot (\varepsilon \rho_f Y_i \vec{V}) = -\nabla \cdot \vec{J}_i + \zeta S_i \tag{5d}$$

$$\sum_{i=1}^{n} Y_i = 1 \tag{5e}$$

$$\rho_f = \frac{p}{R_g T\left(\sum_i Y_i / M_i\right)} \tag{5f}$$

where ζ is set to unity for the flow in a porous medium ($0 < \varepsilon < 1$) and to zero in pure flow regions ($\varepsilon = 1$). F_1 is the Forchheimer coefficient and calculated by $1.8/(180\varepsilon^5)^{0.5}$. $\vec{V}$ is the velocity vector; Y_i is the local mass fraction of component i; ρ_f, K and ε are the fluid density, permeability and porosity of the porous media, respectively. Q_{oh+act} denotes the heat produced by the ohmic and activation losses; Q_{re} is the heat generation by the electrochemical reaction. S_i is the net rate of production of component i by chemical reaction and $\vec{J}_i$ is the diffusion mass flux vector of component i.

2.1.2. Gas transport and concentration overpotential

The gas transport through porous media is mainly controlled by molecular diffusion, Knudsen diffusion and viscous flow. For composite electrodes in fuel cells, the Knudsen diffusion is as important as bulk diffusion due to that the mean free path of molecular species is comparable to the pore size. Thus, the two different diffusion mechanisms should be considered in the present model. Assuming that the porous medium is in local thermodynamic equilibrium with the fluid, the extended Stefan–Maxwell relation is used to determine the diffusion mass flux vector $\vec{J}_i$:

$$\frac{\vec{J}_i}{D_{k,i}} + \sum_{\substack{i=1 \\ j \neq i}}^{n}\left(\frac{X_i\vec{J}_j}{D_{ij,eff}} - \frac{X_j\vec{J}_i}{D_{ij,eff}}\right) = \frac{P}{R_g T}\nabla X_i \tag{6}$$

where X_i is the mole fraction of component i, $D_{ij,eff}$ and $D_{k,i}$ denote the effective binary diffusion coefficient of a mixture of components i and j and the effective Knudsen diffusion coefficient of component i, respectively [34]. The concentration overpotentials, which are induced by the gaseous transport at electrodes and channel flows, are calculated as:

$$\eta_{con}^{ca}(x,y) = \frac{R_g T}{4F}\ln\left(\frac{p_{O_2}^{int}}{p_{O_2}^{r}}\right), \quad \eta_{con}^{an}(x,y) = \frac{R_g T}{2F}\ln\left(\frac{p_{H_2}^{int}}{p_{H_2}^{r}} \cdot \frac{p_{H_2O}^{r}}{p_{H_2O}^{int}}\right) \tag{7}$$

$$\eta_{con}^{fuel} = \frac{R_g T}{4F}\ln\left(\frac{p_{O_2}^{b}}{p_{O_2}^{int}}\right), \quad \eta_{con}^{air} = \frac{R_g T}{2F}\ln\left(\frac{p_{H_2}^{b}}{p_{H_2}^{int}} \cdot \frac{p_{H_2O}^{int}}{p_{H_2O}^{b}}\right) \tag{8}$$

where p_i^b, p_i^{int} and p_i^r ($i = O_2$, H_2O, H_2) are the partial pressures of component i at the air/fuel channel flow, electrode/channel interface and reaction site (TPB), respectively.

2.2. Micro-submodel

There are three different groups of clusters formed in the electrodes: (i) the first is composed of the same type particles (ionic or electronic particles) that are in contact with one another to extend through the entire electrode. This kind of cluster is called the "percolating cluster". It allows different charge to pass throughout the electrode. Under such condition, a good conductivity is reached; (ii) the second is that a cluster is only connected to its corresponding bulk phase type (interconnect or electrolyte); (iii) the third cluster is completely isolated from its corresponding bulk phase. The existence of this kind of cluster increases the polarization resistance in the electrode. In the present micro-porous electrode model, the electronic phase (Ni/LSCF) or ionic phase (SDC) is assumed as formed by the first kind of clusters, which means percolating clusters dominate the electrode performance. This assumption requires the electrodes to have a high ratio of electrode thickness to particle diameter such that this ratio is always greater than 100. When the ratio is lower than 100, the model accuracy may be affected by some degree of uncertainty and the Monte Carlo simulation is therefore suitable for thin electrodes [8,19,35]. The second type is neglected as the ratio of the electrode thickness to particle diameter is assumed to be larger than 100. The third type is included in the current model by parameter choices based on the following derivation. The charge is transferred along the electronic or ionic phase and the transfer current is intrinsically between the two phases.

According to Ohm's law, the current balance in electrodes can be established as:

$$\mathbf{i}_{el} = -\sigma_{el,eff}\nabla V_{el} \tag{9a}$$

$$\mathbf{i}_{io} = -\sigma_{io,eff}\nabla V_{io} \tag{9b}$$

$$\nabla \cdot \mathbf{i}_{io} = -\nabla \cdot \mathbf{i}_{el} = L_{TPB} \cdot i_{tr}^{ca/an}(\eta_{act}, Y_i, T) \tag{9c}$$

where V is the potential and $\mathbf{i}$ ($A\,m^{-2}$) is the current vector per unit area of the electrode. $\sigma_{io,eff}$ and $\sigma_{el,eff}$ are the effective conductivity of the ionic and electronic conductor phase, respectively. L_{TPB} is the active TPB length per unit volume of the electrode. $i_{tr}^{ca/an}$ ($A\,m^{-1}$) is the transfer current density per unit TPB length in the cathode or anode, which is a function of the local activation overpotential $\eta_{act}^{an/ca}$, temperature and concentration. The local activation overpotential η_{act} is equal to:

$$\eta_{act} = (V_{io} - V_{el}) - \eta_{con} \tag{10}$$

The local concentration loss η_{con} is estimated by Eq. (7).

2.3. Model parameters

There are still some unknown parameters or terms to be determined in Eqs. (5) and (9), such as the heat generation sources, the effective conductivities, the TPB length and the transfer current density, etc. The classical percolation theory, coordinate number theory and experimental work on electrode kinetics will be applied to obtain these important parameters.

2.3.1. Effective conductivity and TPB length

According to the results of the percolation theory [36] and the effective medium theory, the effective conductivity of ℓ-phase (ionic or electronic) in a random packing of bimodal particles above the percolation threshold is:

$$\sigma_{\ell,eff} \propto \sigma_{\ell,0}(n - n_c)^m \tag{11}$$

where n_c is the critical number fraction, also called "percolation threshold". At n_c the composite undergoes a phase transition from an insulting to a conducting state, i.e., the minimum volume fraction of ℓ-phase needed for the presence of the first "percolating cluster". The percolation threshold is not expected to be universal, even for regular lattices. m is a phenomenological parameter which depends on the fractal dimension of the electrodes only and always falls in the range 1.2–2.0. n is the number fraction of ℓ-phase. $\sigma_{\ell,0}$ is the conductivity for the ℓ-phase material. Strictly speaking, the percolation equation (Eq. (11)) is only valid for metal-insulator (one of the two phases has zero conductivity) or conductor-perfect conductor (one of the two phases has an infinite conductivity). For real continuum systems, the ratio of conductivities is usually not high enough to enable the percolation equation (11) to be used accurately. To appropriately apply this equation, the number fraction should be far from the percolation threshold. In order to overcome this limitation, several extensions of the classical percolation approach have been proposed [37,38]. Mclachlan [38] proposed an effective general media (EGM) approach to predict the conductivity for composite material containing two components possessing different electrical properties. The Eq. (12) can be used to calculate the conductivity of electrode particle:

$$\sigma_{el,eff} = \sigma_{el,0}\left(1 - \frac{1-\phi_{el}}{1-\phi_{el,c}}\right)^m \tag{12}$$

Similarly, the ionic conductivity for the electrolyte phase is:

$$\sigma_{io,eff} = \sigma_{io,0}\left(1 - \frac{1-\phi_{io}}{1-\phi_{io,c}}\right)^m \tag{13}$$

where ϕ_{el} is the volume fraction of the electrode particles with respect to all solid volume (void excluded). $\phi_{el,c}$ is the volume fraction for electrode particles corresponding to the percolation threshold. $\phi_{io,c}$ is the volume fraction for ionic particles corresponding to the percolation threshold. However, the neck formed between same types of particles reduces this value, so the conductivity can be estimated as:

$$\sigma_{\ell,0} = \sigma_{\ell,bulk}\frac{l_{TPB}}{l_{TPB,max}} = \sigma_{\ell,bulk}\frac{2\pi r_{min}\sin(\gamma/2)}{2\pi r_{min}} = \sigma_{\ell,bulk}\sin\frac{\gamma}{2} \tag{14}$$

where γ is the contact angle and is set as 60° [8,9,18] and r_{min} is the radius of the smaller particle. However, when the porosity is decreased or increased, how is the conductivity in SOFC affected? Here, an approximate approach is introduced to take into account the contribution of pores. According to the Archie's law [39,40], the effective conductivity is strongly dependent on the porosity of the pure materials:

$$\sigma_{\ell,eff} \propto (1-\varepsilon)^t \tag{15}$$

here t is an empirical parameter. For a spherical pore, this value is equal to 1.5 [40]. In actual case, Eq. (12) is obtained with an inherent assumption, i.e., the porosity is estimated as 0.4, so the conductivity of an electrode particle can be modified as:

$$\sigma_{el,eff} = \frac{\sigma_{el,0}(1-\varepsilon)^t}{(1-0.4)^t}\left(1 - \frac{1-\phi_{el}}{1-\phi_{el,c}}\right)^m \tag{16}$$

According to effective medium theory (EMT) [41], the adjustable parameter m also can be chosen as 1.5. Thus the final forms for conductivities are:

$$\sigma_{el,eff} = \sigma_{el,bulk}\sin\frac{\gamma}{2}\left[\frac{1-\varepsilon}{0.6}\cdot\left(1 - \frac{1-\phi_{el}}{1-\phi_{el,c}}\right)\right]^{1.5} \tag{17}$$

Table 1
Model input parameters for the baseline case.

Parameters	Value	Parameters	Value
Fuel inlet temperature (K)	773	Particle/pore size (μm)	1
Air inlet temperature (K)	773	Thermal conductivity for anode ($W\,m^{-1}\,K^{-1}$)	12
Inlet pressure (Pa)	1.01×10^5	Thermal conductivity for interconnector ($W\,m^{-1}\,K^{-1}$)	11
Fuel inlet velocity ($m\,s^{-1}$)	0.5	Thermal conductivity for SDC ($W\,m^{-1}\,K^{-1}$)	2
Air inlet velocity ($m\,s^{-1}$)	2.5	Thermal conductivity for cathode ($W\,m^{-1}\,K^{-1}$)	2.7
Cell length (m)	0.1	Porosity (%)	40
Interconnector height (m)	0.5×10^{-3}	Tortuosity	3.5
Channel height (m)	1.0×10^{-3}	Anode exchange current density ($A\,m^{-2}$)	100
Anode thickness (m)	500×10^{-6}	Cathode exchange current density ($A\,m^{-2}$)	500
Cathode thickness (m)	50×10^{-6}	Electric conductivity for Ni ($S\,m^{-1}$)	$3.27 \times 10^6 - 1065T$
Electrolyte thickness (m)	20×10^{-6}	Ionic conductivity for SDC ($S\,m^{-1}$)	$6.4 \times 10^7/T \times \exp(-86{,}000/8.61734T)$

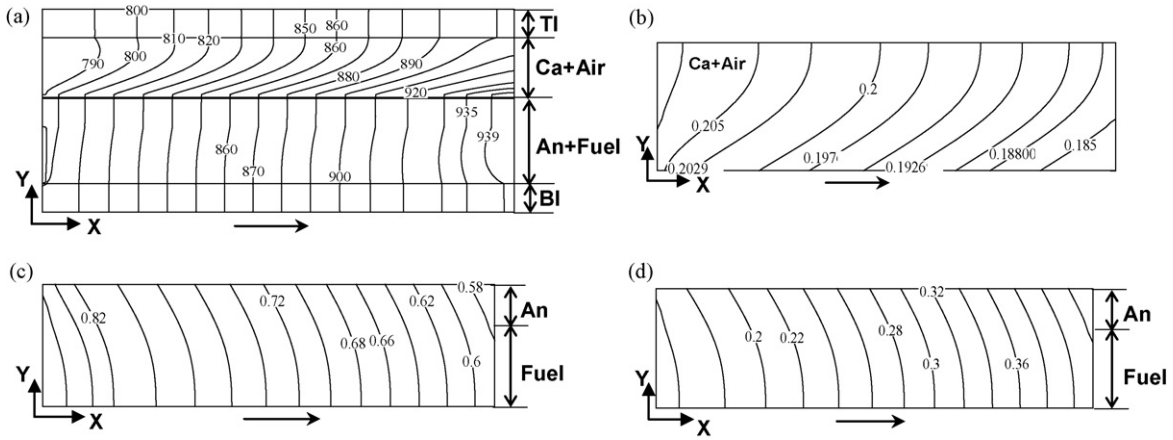

Fig. 2. Temperature and molar contours: (a) temperature, (b) oxygen at air channel and cathode layer, (c) hydrogen at anode layer and fuel channel, and (d) water at anode layer and fuel channel (arrow denotes flow direction; Tl/Bl, top/bottom interconnect; An, anode; Ca, cathode; Air, air channel; Fuel, fuel channel).

$$\sigma_{\mathrm{io,eff}} = \sigma_{\mathrm{io,bulk}} \sin\frac{\gamma}{2}\left[\frac{1-\varepsilon}{0.6}\cdot\left(1-\frac{1-\phi_{\mathrm{io}}}{1-\phi_{\mathrm{io,c}}}\right)\right]^{1.5} \tag{18}$$

In the above equations, the percolation threshold $\phi_{\mathrm{el,c}}$ and $\phi_{\mathrm{io,c}}$ can be determined by the coordination number theory and has been given by [42,43].

The approach to estimate TPB length per unit volume $L_{\mathrm{TPB,V}}$ ($\mathrm{m\,m^{-3}}$) was developed using the relationship between percolation and particle coordination number [18,31,35]:

$$L_{\mathrm{TPB,V}} = 2\pi r_{\min}\sin\frac{\gamma}{2}\cdot N n_{\mathrm{io}} n_{\mathrm{el}} \frac{Z_{\mathrm{io}}Z_{\mathrm{el}}}{Z_0} P_{\mathrm{io}}P_{\mathrm{el}} \tag{19}$$

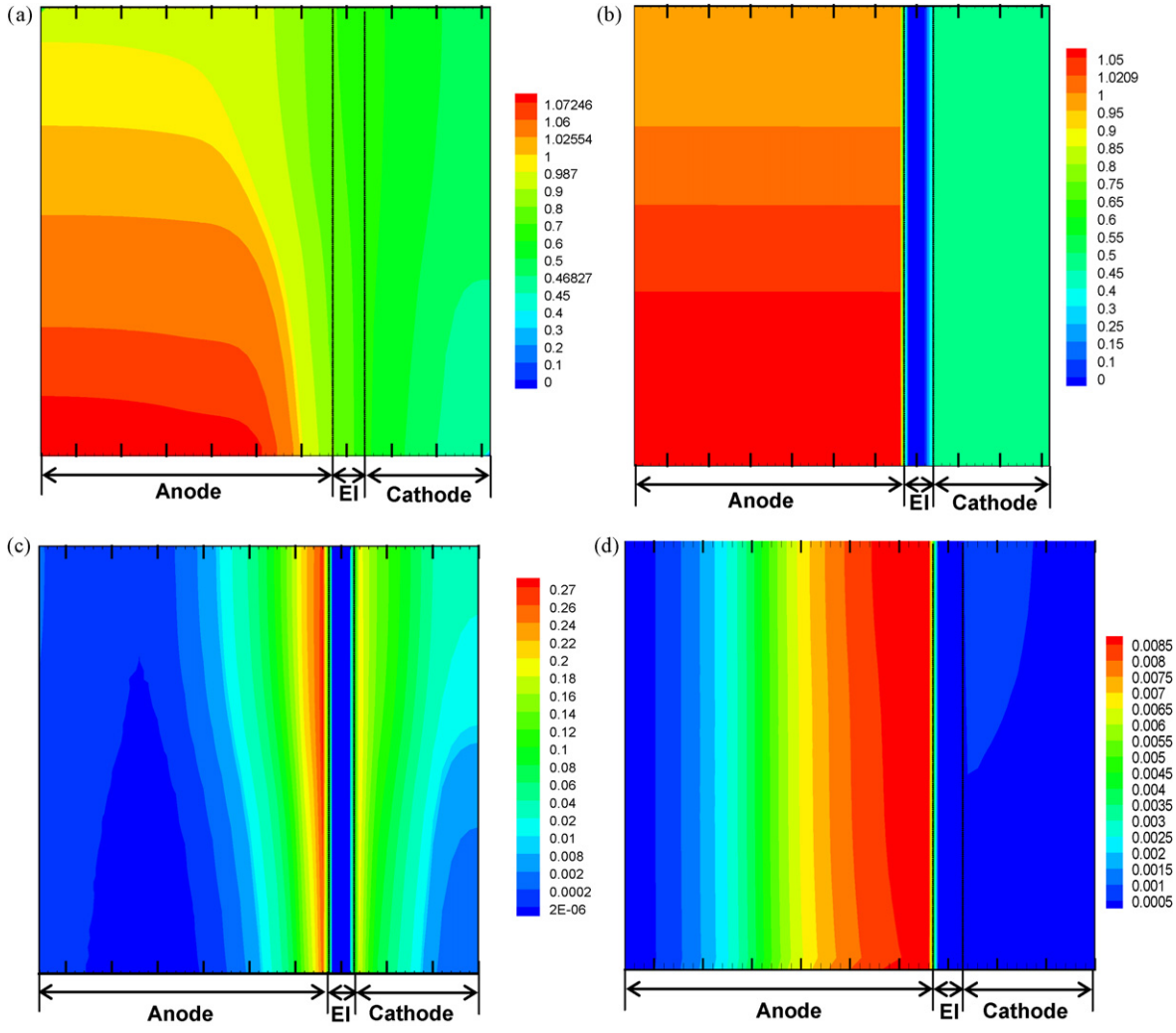

Fig. 3. Performance of SOFC: (a) ionic potential distribution, (b) electronic potential distribution, (c) activation overpotential, and (d) concentration overpotential (unit, V).

where P_{io} and P_{el} are the probability of ionic- or electronic-type conductors in the percolating cluster. Suzuki and Oshima [42] proposed a more accurate expression to P_ℓ in the range $0.154 < \lambda < 6.464$ ($\lambda = d_{io}/d_{el}$ is the diameter ratio between ionic and electronic particles):

$$P_\ell = \left[1 - \left(\frac{4.236 - Z_{\ell-\ell}}{2.472}\right)^{2.5}\right]^{0.4} \tag{20}$$

$$Z_{\ell-\ell} = \frac{Z_0 n_\ell}{n_\ell + (1 - n_\ell)\lambda^2} \tag{21}$$

where $Z_{\ell-\ell}$ is the coordination number between same type particles, and Z_0 is the average total coordination number in a random packing of binomial spheres and equals 6. n_{io} and n_{io} are number fractions of electronic and ionic particles, which are related with volume fractions ϕ_{el} and ϕ_{io}. N is the total number of particles per unit volume. Z_{io} and Z_{el} are the coordination numbers of electronic conductor and ionic conductor. They are given by:

$$N = \frac{1 - \varepsilon}{4/3\pi r_{el}^3 [n_{el} + (1 - n_{el})\lambda^3]} \tag{22}$$

$$Z_{io} = 3 + \frac{(Z_0 - 3)\lambda^2}{n_{el} + (1 - n_{el})\lambda^2} \tag{23}$$

$$Z_{el} = 3 + \frac{Z_0 - 3}{n_{el} + (1 - n_{el})\lambda^2} \tag{24}$$

It should be pointed out that Eqs. (19)–(21) only take into account the contribution of percolating cluster to conductivity and TPB length. As long as ϕ_ℓ is far away from threshold and P_ℓ is also really high, this kind of clusters dominates the response of the electrodes' performance and thus the equations are reasonable.

2.3.2. Electrode kinetics and transfer current density

In principle, oxygen reduction and hydrogen oxidation reactions have been recognized to involve a series of consecutive elemental steps including, i.e., dissociation, charge transfer, surface diffusion of oxygen/hydrogen intermediate species, etc. There is still no common consensus in the mechanisms and kinetics of the two reactions and sometimes contradictory because the elemental steps strongly depend on the specific experimental conditions and microstructure, etc. [44–47]. Especially, the experimental data on electrochemical kinetics of Ni/SDC anode and LSCF/SDC cathode at lower temperatures are very limited and incomplete at present. The relationship between ionic current densities in the composite electrodes and charge-transfer overpotentials can be described by Bulter–Volmer equation:

$$i = i_0 \left\{ \exp\left(\frac{\beta n_e F \eta_{act}}{R_g T}\right) - \exp\left[-(1 - \beta)\frac{n_e F \eta_{act}}{R_g T}\right] \right\} \tag{25}$$

where F is the Faraday's constant. n_e is the number of electrons. β is the transfer coefficient. i_o is the exchange current density, which generally depends on the local temperature and composition in the electrodes. The magnitude of the exchange current density could affect the predominant mechanism. For oxygen reduction in LSCF/SDC cathode, Liu et al. [15] found that the exchange current density i_0^{ca} is between 10 and 650 A m^{-2} at the temperatures ranging from 500 to 700 °C, but they did not further report the effect of the partial oxygen pressure on this value. Here we adopt this range. For SDC/Ni anode under lower operation temperature, the anodic exchange current density is set as 100 A m^{-2} on the basis of literature data [14]. This paper focuses on presenting a theoretical framework instead of making quantitative comparison with experiments, so the constant exchange current densities are still helpful in qualitatively studying the mechanistic issues that govern the performance of SOFCs.

2.3.3. Mass and heat sources

In mass transport Eq. (5d), the net rate of production for each component, S_i, can be stated as the following:

$$S_{H_2O} = M_{H_2O}\frac{1}{2F}\left|\nabla \cdot \mathbf{i}_{el}^{ca}\right| \tag{26a}$$

$$S_{H_2} = -M_{H_2}\frac{1}{2F}\left|\nabla \cdot \mathbf{i}_{el}^{ca}\right| \tag{26b}$$

$$S_{O_2} = -M_{O_2}\frac{1}{4F}\left|\nabla \cdot \mathbf{i}_{el}^{an}\right| \tag{26c}$$

The volumetric heat generated from electrochemical reactions is expressed by:

$$Q_{re} = (\Delta H_{elec} - \Delta G)\frac{1}{2F}\left|\nabla \cdot \mathbf{i}_{el}^{an}\right| \tag{27}$$

Here Eq. (27) is only for anode layer. ΔG is the chemical potential. The heat generated from the ohmic loss, which exists in the electrodes, interconnector and electrolyte, and the activation loss can be expressed by:

$$Q_{oh+act} = [\left|\mathbf{i}_{el} + \mathbf{i}_{io}\right|]^2 \cdot R_{eff} + \eta_{act}^{an/ca} \cdot \mathbf{i}_0 \tag{28}$$

Here R_{eff} is ohmic resistance, which is related to effective conductivity and geometry.

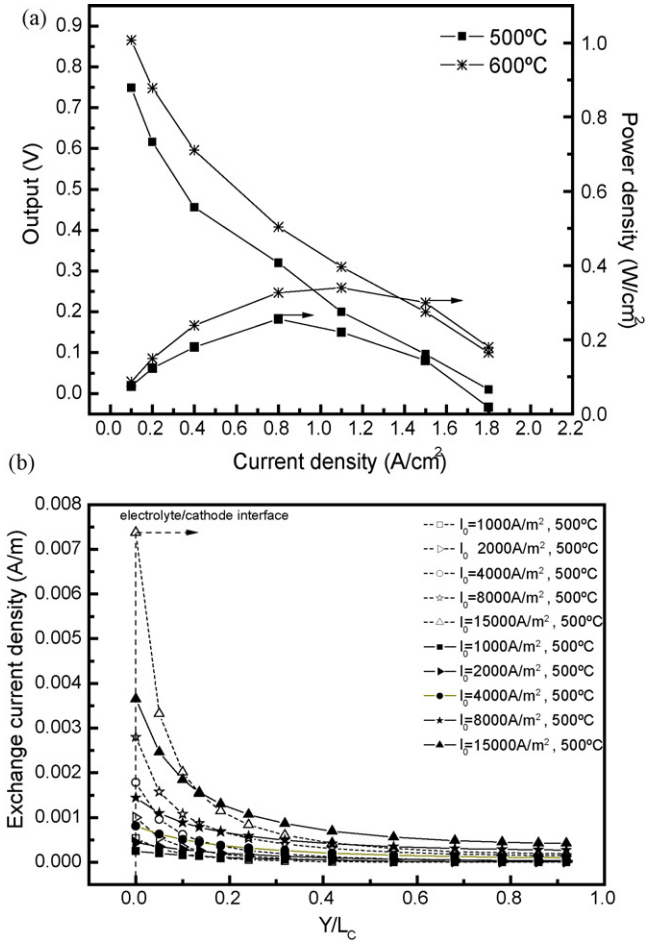

Fig. 4. Performance comparison with 500 and 600 °C: (a) I–V performance and (b) exchange current density distribution over the cathode (I_0 is the average current density).

3. Solution algorithm and parameters

The SIMPLEC [48] method is applied to solve the discretized equations of momentum, energy, concentration and electrical potential. To evaluate the convergence and grid independence of the numerical method and the computational code, we first test it for incompressible gas flow in a smooth microchannel with no slip boundary condition. The numerical results agree well with the analytical results within tolerance criterion. Additional computations were performed with coarse grids and fine grids to check the grid size effect on the numerical solution. The grids are refined near the wall region to obtain possible highly accurate numerical solutions. For example, the grid sizes are set as $50 \times 64 \times 32$, $100 \times 96 \times 48$, and $200 \times 96 \times 64$. The maximal differences between $100 \times 96 \times 48$ and $200 \times 96 \times 64$ grid systems were found negligible. By balancing between the computation time and accuracy, the grid size $100 \times 96 \times 48$ was selected for the computation.

Air (79% N_2 and 21% O_2) is delivered to the air channel. Fuel (85% H_2 and 15% H_2O) is delivered to the fuel channel.

Some input parameters for the baseline case are extracted from the literatures [14–16,49,50] and listed in Table 1. The physical properties of common materials, which are used for electrodes and electrolyte, strongly depend on temperature. Consequently, the performance of a SOFC is affected by the temperature field significantly. For instance, the resistivity of SDC at 1000 K could be one or two orders of magnitude smaller than that at 700 K. This temperature effect is included in the present model. Since low-temperature anode-supported fuel cells are always designed to operate below 1000 K, the inlet fuel and air temperatures are chosen as 773 K in the baseline simulation. The single unit cell is used in the numerical evaluation and the unit is assumed to be placed in an electric furnace exchanging radiation heat transfer between the cell outer surface and the furnace inner surface.

4. Simulation results and discussion

4.1. Baseline Case

To provide a basis for comparison, the thermo-fluid transport and electrochemical performance of an anode-supported SOFC are first investigated using the parameters and operating conditions listed in Table 1. Fig. 2(a) shows the temperature contour along the channel. The temperature at the inlet is set at 773 K and it increases monotonically to around 940 K due to the contribution of Joule heating and chemical reaction. The overall temperature level is considered to be in the low-temperature range of a SOFC operation. On the air side, the temperature rise is not as large as that in the fuel side due to higher mass flow rates. Inside the interconnects, the temperature gradient in the y-direction is fairly uniform due to high thermal conductivity. The molar fraction contours for the major reactants and products at an average current density of 4000 A m^{-2} are plotted in Fig. 2(b)–(d). It reflects a fact that the diffusion of oxygen from the air channel to the cathode creates a significant concentration gradient (Fig. 2(b)). It should be noted that the concentration gradient can be reduced significantly when the oxygen supply is excessive in a practical operation.

On the other hand, the hydrogen and water vapor in the fuel channel do not cause significant concentration gradients in the y-direction since the diffusion of H_2 is about two to three times faster than that of oxygen as Fig. 2(c) and (d) indicate. The molar

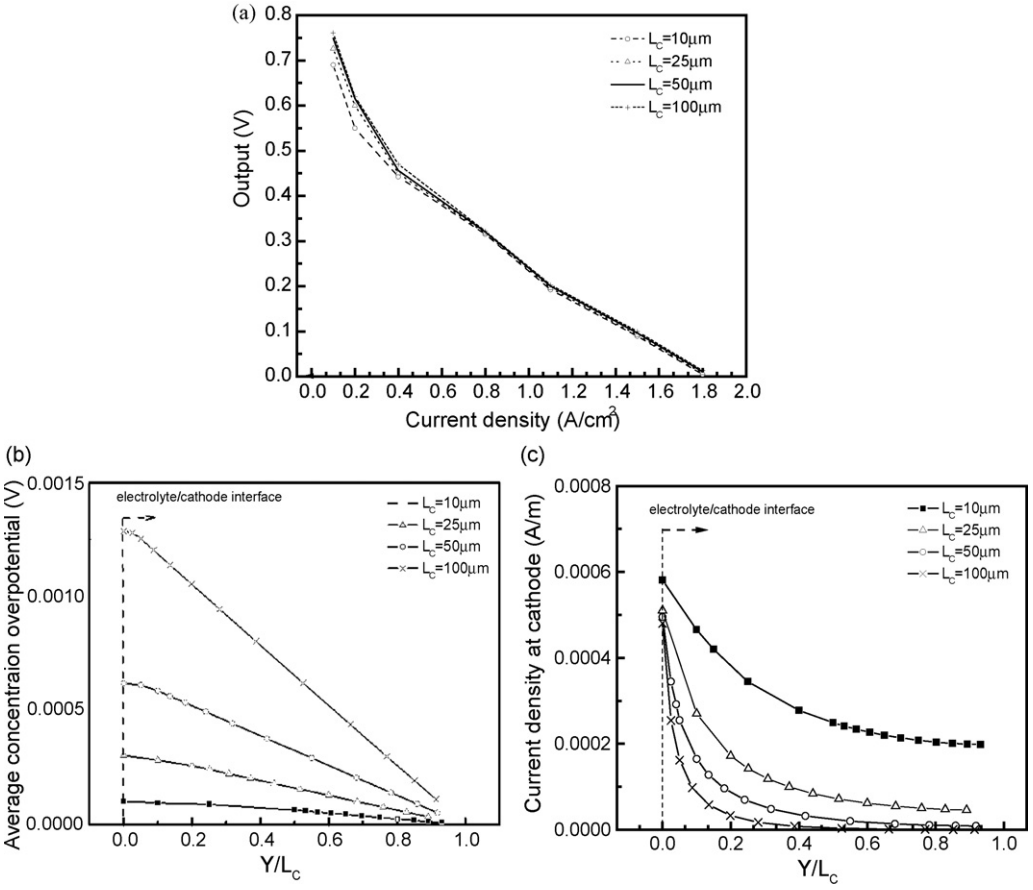

Fig. 5. Effect of cathode thickness on cell performance: (a) I–V performance, (b) concentration overpotential in the cathode, and (c) current density distribution across the cathode.

fraction of H_2 decreases while that of H_2O increases, respectively, from the fuel channel inlet to the outlet due to the electrochemical reaction (Fig. 2(c)). However, in the anode layer, the concentration gradients become significant because of the combination effect of Knudsen diffusion and binary diffusion. The concentration losses at the anode and cathode are detrimental to the cell performance, and it can be minimized by reducing the channel dimension [30,51]. Because the channels with smaller dimensions experience a greater enhancement in the mass and heat transfer rates.

The spatial distributions of electronic and ionic potentials are shown in Fig. 3(a) and (b). In this case, the porosity and the composition ratio of the electrode phase are 0.4 and 0.5, respectively. The terminal output is 0.465 V. It is found that the electronic potential is higher than the ionic potential in the anode and lower than the ionic potential in the cathode as shown in Fig. 3(a) and (b). Moreover, the electronic potential distribution across the cathode and anode is really uniform. While in the ionic phase, it turns out that the potential gradually decreases across the entire fuel cell thickness. These distributions are attributed to the higher conductivity for LSCF/Ni and much lower conductivity for SDC. In the electrolyte, the ionic potential drop is significant (Fig. 3(a)), due to the lower operation temperature as compared with a higher-temperature SOFC. This result implies that the thickness of electrolyte must be minimized for the reduced-temperature fuel cell in order to lower the ohmic overpotential.

Distributions of corresponding activation and concentration polarizations through the cathode and anode are displayed in Fig. 3(c) and (d), respectively. In the cathode, the activation overpotential keeps increasing and reaches the peak value at the interface between the electrolyte and the cathode. This tendency indicates that the strongest electrochemical reaction takes place in the region next to the electrolyte, where the largest potential difference and the maximal current density per unit TPB length exist. This result agrees with those from the previous studies [20,34] using the Monte Carlo simulation. While in the anode, the activation overpotential is almost negligible, i.e., on the order of 10^{-6}, in most of the region and jumps to a remarkable level in the zone next to the electrolyte/cathode interface. This result means a large part of the anode does not actively participate in the electrochemical reaction, i.e., it is useless. Nevertheless, the cathode seems to be much more efficient because the activation overpotential distribution is more even through the entire cathode layer.

The corresponding concentration loss is given in Fig. 3(d). It indicates that this loss is unnoticeable compared with the activation loss in the cathode. But in the anode, the concentration loss becomes substantial and is about ten times larger than that in the cathode due to the larger thickness of anode. Clearly, the activation loss in the cathode contributes most to the overpotential for the current anode-supported low-temperature SOFC unlike in an electrolyte-supported fuel cell, where the ohmic loss is dominant. Therefore, for the current case, the key elements for improving the performance should be focused on optimizing the electrode microstructure.

4.2. Temperature effects

In general, if the operating temperature for a fuel cell is reduced, the performance will deteriorate due to the increase in ohmic loss. In this section, investigation will be carried out to study the dependence of fuel cell performance on the gas inlet temperature. Two gas inlet temperatures of 500 and 600 °C are investigated. The other input parameters and properties are still kept the same as those in the baseline case. The simulated performance is shown in Fig. 4(a) and (b). They indicate that the maximum power density is about 0.256 W cm^{-2} for 500 °C and 0.34 W cm^{-2} for 600 °C. The terminal output is about 0.749 V for 500 °C and 0.866 V for 600 °C. Compared with the higher operating temperature SOFC such as an electrolyte-supported fuel cell, this kind of reduced-temperature fuel cells has a relatively lower performance due to a higher ohmic loss and a weak electrochemical reaction activity. The corresponding current density distribution is displayed in Fig. 4(b). Clearly, the electrochemical reaction strongly depends on the temperature. As the temperature is increased to 600 °C, the profiles of exchange current density in the cathode become flattened, which means more regions are involved in the reaction and the cathode becomes more efficient. Another point is that as the current density increases, the relative importance of TPB near the electrolyte becomes more prominent, and the region far away from the electrolyte is almost "useless" having the weakest reaction rate. Similar case holds for the anode, but the useless region in the anode is much larger.

4.3. Thickness optimization

In order to study the dependence of SOFC performance, overpotential and exchange current density (or reaction activity) on the electrode thickness, several cases with different cathode and anode thicknesses are carried out. Fig. 5 presents the comparison results for different cathode thicknesses. The *I–V* performance curves in Fig. 5(a) exhibit insignificant dependence on the cathode thickness. When the current density is lower, i.e., 1000 or 2000 A m^{-2}, the performance is enhanced with a larger cathode thickness, but it is not remarkable. When the current density exceeds 8000 A m^{-2}, such

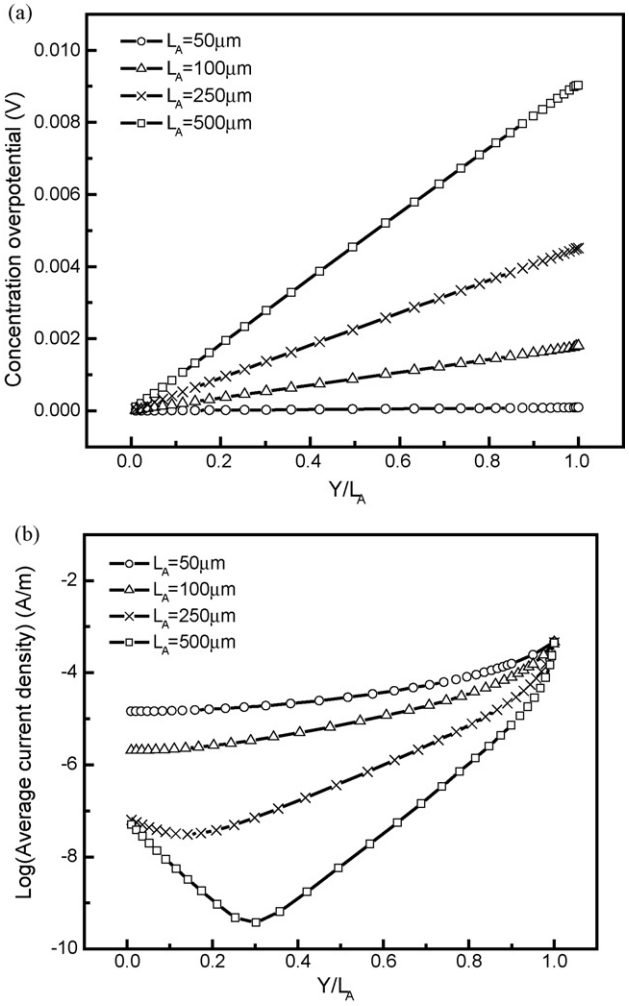

Fig. 6. Effect of anode thickness on cell performance: (a) concentration overpotential in the anode and (b) current density distribution across the anode.

differences are so unnoticeable that the curves are almost identical. A thicker cathode possesses increased TPB number that results in the improvement of the activity of chemical reaction; on the other hand, the concentration overpotential also is increased at the same time as shown in Fig. 5(b). However even for a thicker cathode, the concentration loss in the cathode is still insignificant, e.g., in the order of 10^{-3}–10^{-4} V, so the decrease in activation loss overweighs the increase in concentration loss and the overall cathode performance is better when the current density is not very high. Although for a thicker cathode, the concentration overpotential starts to become significant due to a longer diffusion path as the current density is very high, such increase still is not so substantial that it can be completely counteracted by the reduction in activation overpotential. Additionally, the temperature rise in a thicker cathode is slightly larger, which offers an extra improvement in the performance to some extents.

Fig. 5(c) shows that a thinner cathode provides a much more uniform density distribution and thus results in higher cathode utilization. However, after we review the results from Fig. 5(a) that an extremely thin cathode (e.g., 10 μm) has an overall lower performance due to insufficient reaction sites, it is suggested that the cathode thickness should be between 25 and 100 μm to achieve an optimal combination of a minimized concentration loss and a uniform reaction rate. These results are in good agreement with the previous theoretical studies [18,21]. Experimental results [52] also demonstrated that the thickness of a cathode must exceed a certain value to achieve an optimal performance with a decreased polarization resistance. For the anode, similar results can also be obtained as illustrated in Fig. 6. But the difference is that the concentration overpotential becomes more significant than that in the cathode, especially for the case of a higher current density. For the thicker anodes, valley regions occur and the central part of anode layer cannot be utilized very well due to the limitation of mass diffusion. However, the electrochemical reaction seems to occur throughout the whole anode at thickness less than 100 μm.

4.4. Porosity

In this section, the effect of electrode porosity on the fuel cell performance is investigated. A more realistic electrode geometry is considered by setting the anode and cathode thickness as 500 and 50 μm, respectively. The porosity is varied between 0.25 and 0.6. Fig. 7(a) gives the dependence of *I–V* performance on the porosity. It turns out that reducing the electrode porosity leads to a slight increase in terminal output for both cathode and the anode. On the one hand, a smaller porosity leads to an increase in solid volume fraction and thus TPB length, so the activation overpotential is effectively decreased as shown in Fig. 7(b) and (c).

In particular, the reduction of activation overpotential in the cathode is much more remarkable, which leads to a higher performance improvement in the cathode than that in the anode. However, on the other hand, an extremely small porosity limits the mass transfer from the channels to the reaction sites and increases the concentration loss and pressure loss in the electrodes by reducing the binary diffusivity, Knudsen diffusivity and permeability. This negative effect becomes severe for the anode with a larger current density, 11,000 A m^{-2}, so the anode with the smallest porosity 0.25 does not have too much improvement compared with that with porosity 0.3. Therefore, it is not desirable to improve the fuel cell efficiency by reducing porosity, because it causes a larger mass transport loss and pressure loss in the porous anode layer. This is the main reason why the porosity is always in the range of 0.3–0.4 in the practical application. In the previous study based on the Monte Carlo simulation [19,35], gas is assumed to penetrate into the anode

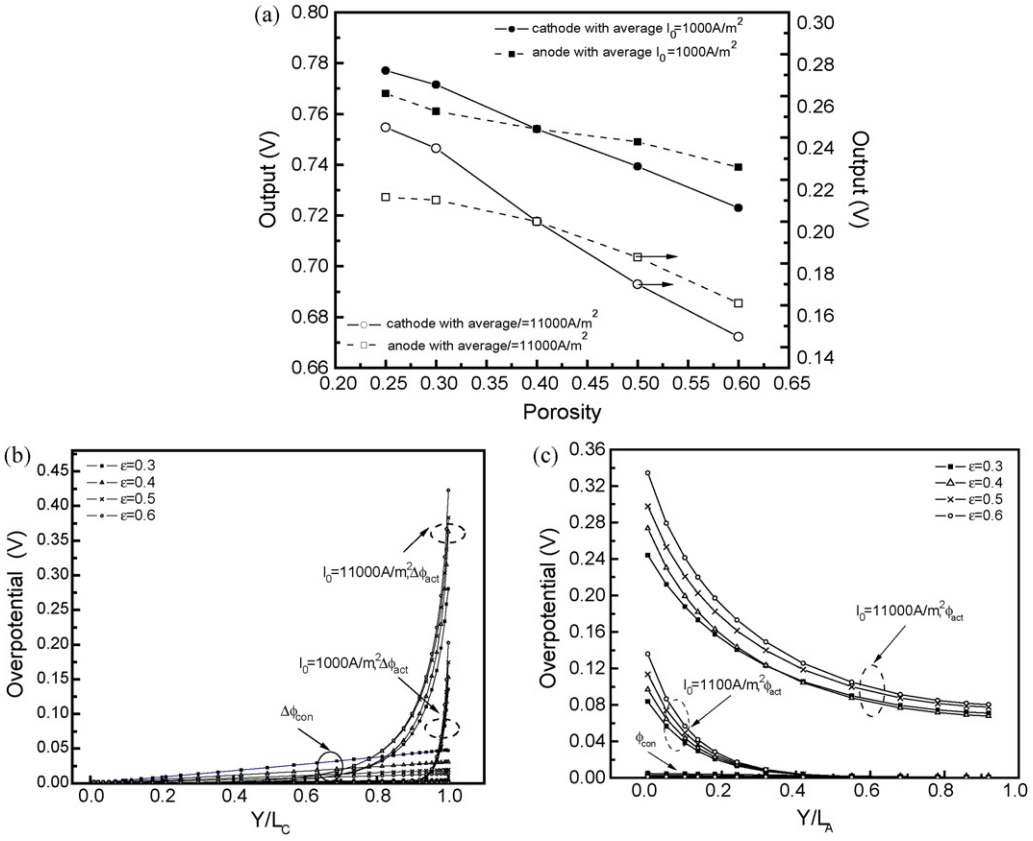

Fig. 7. Effect of electrode porosity on performance and overpotentials: (a) dependence of *I–V* performance on the porosity, (b) overpotentials for cathode, and (c) overpotentials for anode (I_0 is the average current density).

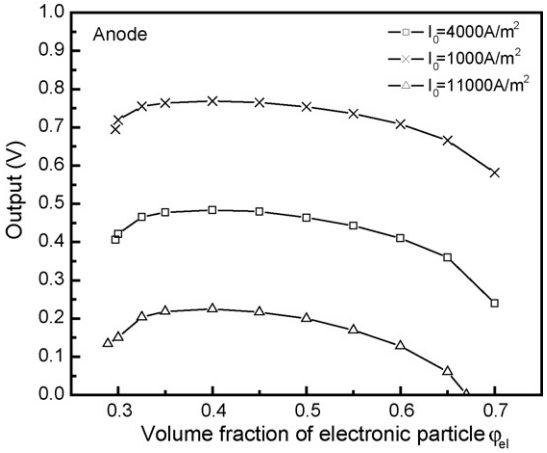

Fig. 8. Effect of anode composition on performance.

or cathode and also include the "dead effect" or "inactive TPB". However, in the current study, it is assumed that all pores are open to gas reaction and not any dead effects, so the decreasing of output is just caused by the decreasing of TPB length and the concentration effect is not very significant.

4.5. Electrode composite

First of all, it should be noted that the continuum theory and coordination number theory have demonstrated that the percolation threshold varies from 0.294 to 0.709 as the radius ratio equals to unity. Therefore, the current model based on the two theories is invalid beyond this percolation range. In the study of the composition effect, the volume fraction number of the electronic phase ranges between 0.299 and 0.7. Fig. 8 presents the effect of electronic phase volume fraction in the anode on the terminal output. The maximal performance is achieved at φ_{el} = 0.4–0.45. For cases with $0.297 < \varphi_{el} < 0.35$ and $0.5 < \varphi_{el} < 0.7$, the output is relatively lower; it means the charge resistance is greatly increased due to insufficient reaction sites and smaller TPB length. For the cathode, further calculation also shows the similar optimal value. These results match well with the previous experimental and theoretical results [18]. However, when the composition is beyond the percolation threshold, our previous study has indicated that the specific total resistance is very large and the overall performance deteriorates.

4.6. Particle diameter

Fig. 9 shows the influence of particle size on the terminal output and exchange current density for ionic and electronic phases. The thicknesses of cathode and anode still are kept as 50 and 500 μm, respectively. From Fig. 9(a), it is observed that a smaller particle diameter results in better performance, primarily due to the increase of the active three phase boundary length per unit volume. However, the improvement is less significant at the lower average current density, e.g., 1000 A m^{-2}, which is due to the relatively smaller contribution of activation overpotential to the overall potential loss.

Apparently for the larger particle size and the smaller density of TPBs, the exchange current density per unit length is higher

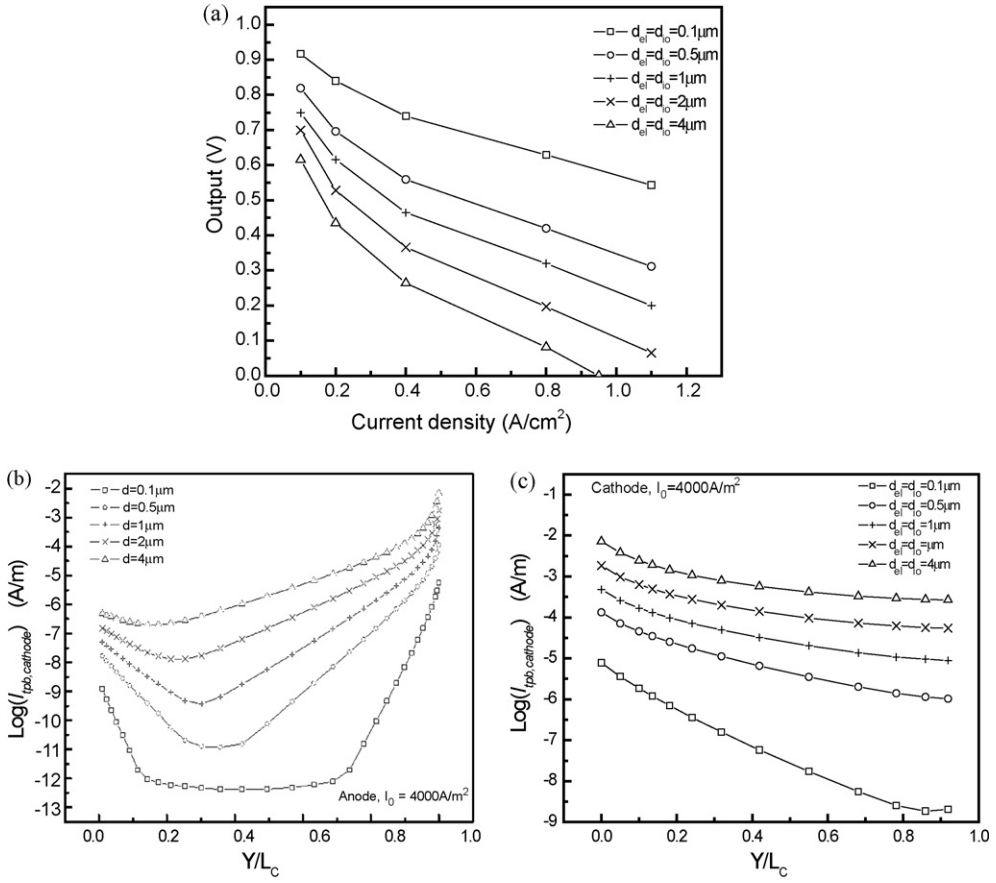

Fig. 9. Effect of particle sizes on performance: (a) *I–V* performance, (b) averaged exchange current density distribution across the anode, and (c) averaged exchange current density distribution across the cathode.

which is due to the conservation of charge. For the anode with the smallest particle size, i.e., 0.1 μm, only the end regions of the anode play important roles in generating the current and so the electrode reaction mainly occurs in the reaction zone close to the anode/electrolyte and anode/fuel interfaces. In particular, the anode/electrolyte zone is much more remarkable. If comparing Fig. 9(b) with Fig. 6(b), the valley region shrinks with increasing particle sizes. It indicates that a larger particle size improves the activity of the electrochemical reaction at the TPBs and the reaction is much more uniform across the whole anode. Similarly, if the particle size in the cathode is extremely small, the zone close to the electrolyte/cathode interface plays a significant role. With the increase of particle radius, the reaction zone extends into the bulk of the composite cathode due to the decrease of the active length of TPB. In addition, extremely small particle sizes will have very small pore sizes in electrodes and results in high concentration overpotentials. Therefore, Fig. 9(b) and (c) can be considered as useful criteria to determine the electrode thickness with different particle sizes.

5. Conclusion

A physical model that consists of two submodels, i.e., a micro-scale submodel and a macro-scale submodel has been developed for the investigation of a low-temperature SOFC. The macro-scale submodel is based on the continuum conservation laws. The micro-scale submodel addresses the complex relationships among the transport phenomena in the electrodes and electrolyte, which include the transport of electrons, ions and gas molecules through the composite electrodes, electrolyte and three-phase boundary region. The model was used to assess the dependence of electrochemical performance on the temperature, global geometrical parameter and material microstructures (porosity, volume fraction, composite ratio, etc.). The important findings are listed below:

- For the current low-temperature, anode-supported fuel cell, a major portion of the overpotential comes from the activation loss in the cathode.
- In general, when the system operating temperature is lowered, the performance is reduced mainly due to the increased ohmic loss in the electrolyte layer and reduced electro-chemical reactivity which renders portions of the electrodes inactive. Either new materials or reducing the layer thickness is needed.
- In order to balance the competing effects, the cathode thickness is suggested to be in the range of 25–100 μm. For the anode, the thickness should be limited to some certain value in order to avoid excessive concentration loss and lower utilization.
- When the porosity is reduced, the activation overpotential is lowered but the concentration loss and pressure drop are increased. The optimal range for the porosity is between 0.3 and 0.4.
- The optimal electronic phase volume fraction is determined in the range of 0.35–0.5.
- In general, the fuel cell performance increases as the particle size is reduced. While larger particles produce wider reaction zones and more uniform activities.

Acknowledgements

This research was supported by the NASA Hydrogen Research for Spaceport and Space Based Applications at the University of Florida (Grant Number NAG3-2930). The support by the Andrew H. Hines, Jr./Progress Energy Endowment Fund is also acknowledged.

References

[1] J. Larminie, A. Dicks, Fuel Cell Systems Explained, 3rd ed., John Wiley & Sons Inc., Chichester, West Sussex, 2003.
[2] S.C. Singhal, K. Kendall, High Temperature Solid Oxide Fuel Cells, Elsevier, New York, 2003.
[3] Z. Cai, T.N. Lan, S. Wang, M. Dokiya, Solid State Ionics 152/153 (2002) 583–590.
[4] R. Kungas, I. Kivi, K. Lust, J. Electroanal. Chem. 629 (2009) 94–101.
[5] S. Sugita, Y. Yoshida, H. Orui, J. Power Sources 185 (2008) 932–936.
[6] T. Tsai, S.A. Barnett, Solid State Ionics 98 (1997) 191–196.
[7] J.L. Hertz, H.L. Tuller, Electroceramics 13 (2004) 663–668.
[8] X. Chen, N.J. Wu, L. Smith, A. Ignatiev, Appl. Phys. Lett. 84 (2004) 2700–2702.
[9] X.J. Chen, S.H. Chan, K.A. Khor, Electrochim. Acta 49 (2004) 1851–1861.
[10] Z. Shao, S.M. Haile, J. Ahn, P.D. Ronney, Z. Zhan, S.A. Barnett, Nature 435 (2005) 795–798.
[11] S. Wang, M. Ando, T. Ishihara, Y. Takita, Solid State Ionics 174 (2004) (2004) 49–55.
[12] X. Zhang, M. Robertson, S. Yick, C. Deces-Petit, E. Styles, W. Qu, Y. Xie, R. Hui, J. Roller, O. Kesler, R. Maric, D. Ghosh, J. Power Sources 160 (2006) 1211–1216.
[13] B.P. Gorman, H.U. Anderson, J. Am. Ceram. Soc. 88 (2005) 1747–1753.
[14] M. Watanabe, H. Uchida, M. Yoshida, J. Electrochem. Soc. 144 (1997) 1739–1743.
[15] J. Liu, A.C. Co, S. Paulson, V.I. Birss, Solid State Ionics 177 (2006) 377–387.
[16] W. Huang, P. Shuk, M. Greenblatt, Solid State Ionics 100 (1997) 23–27.
[17] M. Ni, M. Leung, D. Leung, J. Power Sources 168 (2007) 369–378.
[18] P. Costamagna, P. Costa, V. Antonucci, Electrochim. Acta 43 (1998) 375–394.
[19] S. Sunde, J. Electroceram. 5 (2000) 153–182.
[20] J.H. Nam, D.H. Jeon, Electrochim. Acta 51 (2006) 3446–3460.
[21] D.H. Jeon, J.H. Nam, C.J. Kim, J. Electrochem. Soc. 153 (2006) A406–A417.
[22] G. Wang, P.P. Mukherjee, C.Y. Wang, Electrochim. Acta 51 (2006) 3139–3150.
[23] G. Wang, P.P. Mukherjee, C.Y. Wang, Electrochim. Acta 51 (2006) 3151–3160.
[24] B. Kenney, M. Valdmanis, C. Baker, J. Power Sources 189 (2009) 1051–1059.
[25] Y. Zheng, R. Ran, H.X. Gu, J. Power Sources 185 (2008) 641–648.
[26] M.M. Hussain, X. Li, I. Dincer, J. Power Sources 189 (2009) 916–928.
[27] S. Kapadia, W.K. Anderson, J. Power Sources 189 (2009) 1074–1082.
[28] D.H. Jeon, Elecrochim. Acta 54 (2009) 2727–2736.
[29] Y. Yang, G. Wang, H. Zhang, W. Xia, J. Power Sources 173 (2007) 233–239.
[30] Y. Ji, K. Yuan, J.N. Chung, Y.C. Chen, J. Power Sources 161 (2006) 380–391.
[31] D. Bouvard, F.F. Lange, Acta Metall. Mater. 39 (1991) 3083–3090.
[32] W.G. Bessler, S. Gewies, M. Vogler, Electrochim. Acta 53 (2007) 1782–1800.
[33] A. Smirnov, A. Burt, I. Celik, J. Power Sources 158 (2006) 295–302.
[34] Y. Ji, K. Yuan, J.N. Chung, J. Power Sources 165 (2007) 774–785.
[35] S. Sunde, J. Electrochem. Soc. 143 (1996) 1123–1132.
[36] S. Kirkpatrick, Rev. Mod. Phys. 45 (1973) 574–588.
[37] F. Lux, J. Mater. Sci. 28 (1993) 285–301.
[38] D.S. Mclachlan, J. Phys. C: Solid State Phys. 19 (1986) 1339–1354.
[39] G.E. Archie, Trans. Am. Inst. Min. Metall. Eng. 146 (1942) 54–62.
[40] P. Wong, J. Koplik, J.P. Tomanic, Phys. Rev. B 30 (1984) 6606–6614.
[41] D.S. Mclachlan, M. Blaszkiewicz, R.E. Newhanm, J. Am. Ceram. Soc. 73 (1990) 2187–2203.
[42] M. Suzuki, T. Oshima, Power Technol. 35 (1983) 159–166.
[43] C. Kuo, P.K. Gupta, Acta. Metall. Mater. 43 (1995) 397–403.
[44] A. Bieberle, L.P. Meier, L.J. Gaucker, J. Electrochem. Soc. 148 (2001) A646–A656.
[45] J. Fleig, Annu. Rev. Mater. Res. 33 (2003) 361–382.
[46] S.B. Alder, Chem. Rev. 104 (2004) 4791–4843.
[47] Y. Jiang, S. Wang, Y. Zhang, J. Yan, W. Li, Solid State Ionics 110 (1998) 111–119.
[48] S.V. Patankar, Numerical Heat Transfer and Fluid Flow, Hemisphere Press, New York, 1980.
[49] Z. Zhan, T. Wen, H. Tu, Z. Lu, J. Electrochem. Soc. 148 (2001) A427–A432.
[50] U. Anselmi-Tamburini, G. Chiodelli, M. Arimondi, F. Maglia, G. Spinolo, Z.A. Munir, Solid State Ionics 110 (1998) 35–43.
[51] S.W. Cha, R. O'Hayre, S.J. Lee, Y. Saito, F.B. Prinza, J. Electrochem. Soc. 151 (2004) A1856–A1864.
[52] T. Kenjo, S. Osawa, K. Fujikawa, J. Electrochem. Soc. 138 (1991) 349–356.